

Domain Walls Stabilized by Intrinsic Phonon Modes and Engineered Defects Enable Robust Ferroelectricity in HfO₂

Chenxi Yu,^{1,*} Jiajia Zhang,^{1,*} Xujin Song,^{1,*} Dijiang Sun,¹ Shangze Li,¹ Fei Liu,^{1,†} Xiaoyan Liu,¹ Wei Xi,^{2,‡} and Jinfeng Kang^{1,§}

¹*School of Integrated Circuits, Peking University, Beijing, China*

²*Advanced Instrumental Analysis Center,*

School of Chemical Engineering and Technology,

Tianjin University, Tianjin, China

Abstract

Ferroelectric HfO_2 has attracted extensive research interest for its applications in AI era. The domain walls play a crucial role in phase structure stabilization and polarization switching of ferroelectric HfO_2 , however, a thorough understanding is still lacking. Here, we developed a unified framework based on phonon mode expansion to systematically study the effects of phonon modes and defects on domain wall structures. Using this approach combined with first-principle calculations, we revealed that the interface phonon modes play a key role in stability of domain walls; defects pin and stabilize ferroelectric domains, which in turn stabilizes the metastable orthorhombic phase and facilitates polarization switching. This provides an insight from the microscopic physics origin into the enhanced ferroelectricity in HfO_2 by doping and defect engineering. Furthermore, the theoretically predicted domain structures and defect distributions were observed in La-doped HfO_2 ferroelectric films by EELS and STEM experiments, which confirms the validity of our findings.

Since the discovery in 2011 [1], HfO_2 -based ferroelectrics have attracted much research interests for its CMOS-compatibility [2–4] (complementary metal oxide semiconductor), strong ferroelectricity in nano-scale [3, 5–7] which make it a promising candidate for applications in non-volatile memory and compute-in memory devices in artificial intelligence (AI) era. Tremendous efforts have been made to explore the physical origin of ferroelectricity in HfO_2 -based ferroelectrics, including the formation of ferroelectric orthorhombic phase (OIII phase) [8], the formation of rhombohedral phase [9, 10] and the ferroelectricity induced by ordered oxygen vacancies [11, 12]. Most of the existing experiments and theoretical works support the formation of OIII phase as the origin of ferroelectricity in HfO_2 thin films [13–16]. However, OIII phase is a meta-stable phase under ambient conditions. The ground state is achieved in monoclinic phase (M phase) from both theory [8, 17] and experiments [18]. Researchers found that there are various factors existing in thin films that can stabilize the ferroelectric OIII phase, including the strain [19–22], interface [23, 24] and defects [25–31]. Most existing researches on stabilizing factors focused on phase stability, switching barrier, kinetical stability and ferroelectric cycling behaviors, which are studied from the view of energy landscape. Although the stabilization of ferroelectric phase has been well-established from an energy landscape perspective in existing studies, its implications for device-relevant

behavior, especially the dynamics of ferroelectric switching, are not well understood. The domain walls (DWs) are one of the key features of ferroelectrics that have significant influence on polarization switching, which is attracting more and more interests in the study of ferroelectric HfO₂ recently [32–35]. Therefore, the study of DWs may bridge the gap by providing a microscope view of robust ferroelectricity in HfO₂. Previous researches focused on the dependence of DW stability and polarization switching path [32, 33, 35]. They found that there are different types of DWs that have different stability and switching barriers. Recent studies found the crucial role of defects in DW stability by lowering the DW energy [36–39]. The defects in ferroelectric HfO₂ thin films are dopants and oxygen vacancy, the intrinsic defect that widely exist in HfO₂ thin films [15, 40]. The defects are proved to be important impact factors in stabilizing OIII phase [15, 16, 41]. Although there are already plenty of researches on DW stability and switching, a thorough research on DW stability and the impact of defects is still lacking. One of the obstacles is that the classification of DWs is a tedious task due to the 48 variants of OIII unitcells. These 48 OIII unitcell variants are linked by symmetry transformation under the $Fm\bar{3}m$ space group of cubic phase, therefore, the concept of pseudo-chirality is introduced to distinguish the eight OIII unitcell variants with a fixed polarization direction from six possible polarization directions [20, 32, 35]. The large number of OIII unitcell variants is originated from the low space group symmetry of OIII phase. By analysing the phonon spectrum, the low-symmetry OIII unitcells can be generated from the high-symmetry cubic unitcells by the phonon modes including soft modes and hard modes [20, 34, 42–44]. After analysing the phonon mode amplitudes of OIII unitcell with various pseudo-chiralities, we found that there is a one-to-one correspondence between the mode amplitudes and pseudo-chiralities, which makes it possible to represent the pseudo-chirality using phonon mode amplitudes. The mode amplitudes can be obtained by expanding the atomic coordinates of OIII unitcells using a complete basis of phonon modes. In this work, we developed a method based on phonon mode expansion to systematically study the effects of phonon modes and defects on domain wall structures. This method based on mode expansion is discussed in detail in our complementary work [45]. Using this method, we classified all inequivalent DWs, and studied the effects of phonon modes and defects on DW structures using first-principle calculations. We found that the stability of unstrained DWs is determined by the polarization and pseudo-chirality of domains which are related to the phonon mode characteristics. The DWs act as the critical intermediary

through which defects impact the stability of OIII phase by pinning the DWs and increasing DW stability. The defects concentrated on the DW can facilitate DW switching through DW motion from the DW interface by lowering the switching barrier [46–48]. Furthermore, we conducted EELS analysis and STEM characterization to observe the distribution of defects and the DW structures in La-doped ferroelectric HfO₂ thin films to confirm our findings.

Firstly, we defined eight pseudo-chirality numbers of OIII unitcell to represent the pseudo-chirality of domains in DWs. The pseudo-chirality has a one-to-one correspondence to the mode amplitudes, therefore, we made the mode expansion of atom displacements in OIII phase relative to that of cubic phase. We calculated the phonon spectrum of cubic phase using the conventional cubic unitcell, and extracted all the modes on the Γ point of cubic conventional cell. We found that the modes of the sixth branch can uniquely determine the pseudo-chirality of OIII unitcell, which is shown in Equation 1. The sixth branch has degeneracy of six and irreducible representation of X_5 , whose mode amplitudes are denoted by $Q_{6zx}, Q_{6xy}, Q_{6yz}, Q_{6yx}, Q_{6zy}, Q_{6xz}$, where the first subscripts x, y, z indicate that the phonon mode is folded from X, Y and Z point in the primitive Brillouin zone and the second subscripts x, y, z indicate the direction of atom displacements.

$$\begin{aligned} Q_6(\text{OIII,primary}) &= 0.052 (\epsilon_1 Q_{6zx} + \epsilon_2 Q_{6xy} + \epsilon_3 Q_{6yz}) \\ Q_6(\text{OIII,conjugate}) &= 0.052 (\epsilon_1 Q_{6yx} + \epsilon_2 Q_{6zy} + \epsilon_3 Q_{6xz}) \end{aligned} \tag{1}$$

These Q_6 modes appear in two triplets which are C_4 -conjugated and denoted the primary and conjugate triplets. Using the two types of triplets and three signs $\epsilon_1, \epsilon_2, \epsilon_3$, we can define eight pseudo-chirality numbers in Table I which are related to phonon modes of OIII phase by the mode expansion expression of Equation 1. The detailed discussion on the mode expansion approach is shown in our complementary work [45].

Using the pseudo-chirality number and polarization direction, we enumerated all the inequivalent DWs and studied effect of modes on their stability. We constructed the DW model comprised of two domains as shown in Fig. 1a. The DWs with interface along one of (100), (010) and (001) directions have seven inequivalent polarization configurations as shown in Fig. 1b, with two types of 0° DWs, two 180° DWs and three 90° DWs. We used first-principle calculations by VASP software [49, 50] to do structure relaxation of these DWs. Some DWs are not stable after structure relaxation, which can be classified into these cases: the transition into single-domain structure; the transition from orthorhombic

TABLE I. Signs and conjugate pairs in mode expansion of OIII and the definition of (pseudo-) chirality number

Chirality Number	Primary/Conjugate	ϵ_1	ϵ_2	ϵ_3
0	P	+	+	+
1	P	+	-	-
2	P	-	+	-
3	P	-	-	-
4	C	+	+	+
5	C	+	-	-
6	C	-	+	-
7	C	-	-	+

phase to monoclinic phase or tetragonal phase; the motion of DW by half-cell, increasing or decreasing domain size by half-integer; and the destruction of the whole superstructure. We found that the stability of DWs is related to the dipole configuration and the pseudo-chirality number of two domains, which are directly related to interface phonon modes. Fig. 1c shows the dependence of DW stability on dipole configuration and pseudo-chirality number of two domains. From these stability maps, we can summarize some stability rules:

1. The number of stable DWs depends on the angle between polarization vectors, following the order: $0^\circ > 180^\circ > 90^\circ$.
2. The 180° DW with two polarization vectors parallel to normal vector is not stable.
3. The 90° DW with two Q_1 modes parallel to each other is not stable.
4. Other individual unstable cases.

The first rule has these origins: the 0° DW has less dipole interaction energy than 180° DW and 90° DW; 90° DW has larger lattice mismatch than 0° DW and 180° DW; and different mode interactions in 180° DW and 90° DW. The second rule is related to the DW charges. The 180° DW with two polarization vectors parallel to normal vector has the largest interface charge density, therefore, it is the most unstable DW. The 90° DW with one polarization vector normal to interface has half the interface charge density as the

most unstable 180° DW, as a consequence, it is the second most unstable DW. However, we observed many 90° DWs in experiments [51], including that with one polarization vector normal to interface, which seems contradictory to our finding. In fact, these DWs are stabilized by defects, which modulate the mode interactions at interface and reduce interface charges [36]. The third rule is related to interface mode interactions, causing the instability at these regions where the two Q_1 modes are parallel to each other: the left-upper corner in the stability map of dipole configuration b, a ; and the left-upper, left-bottom and right-bottom corners of dipole configuration b, c and b, \bar{c} . This rule is not strictly obeyed by DWs with defects which modulate the mode interactions, but the DWs following this rule can be stabilized by more defect arrangements than those not following this rule.

From the above analysis of phonon mode effect, we found that the defects play an important role on the stabilization of DW besides the modes. Due to the trivalent nature of La, the doping of La introduces oxygen vacancies V_O into HfO_2 for charge compensation. We calculated the formation energy of La_{Hf} and V_O defect pairs versus the distance between the defect pairs as shown in Fig. 2a, and found that the formation energy has a positive correlation with the defect distance, which indicates that the V_O has a high probability to form near the La dopant. Next, we studied the distribution of defects inside the domain structure. We constructed the DW model comprised of two domains as in Fig. 2b, with one of the domains have La_{Hf} and V_O defects. The DW energy versus the distance from defects to DW interface in Fig. 2c shows that the lowest energy configuration is achieved when the defects are at the interfaces, or the defects have a pinning effect on the DW interfaces. Based on this defect pinning effect, we calculated the stability map of DWs with defects by adding defects at the DW interfaces. We chose the 90° DWs which are the most unstable without defects to calculate, and the results are shown in Fig. 2d that the defects can stabilize most of the DWs that are not stable without defects. It is worth to mention that the stabilized 90° DW by certain arrangement of defects may not be stable by other arrangements of defects. This fact may be caused by the artifacts of three-dimensional periodic condition used in calculation, even though we made 2×2 supercell in two interface directions, the structure is still not large enough for simulation. Also, this fact implies that the ferroelectricity of HfO_2 is intertwined to defects [11, 28, 52–55].

Subsequently, we studied the switching of DW using first-principle calculation. Using mode expansion method, we enumerated all the inequivalent switching paths and summa-

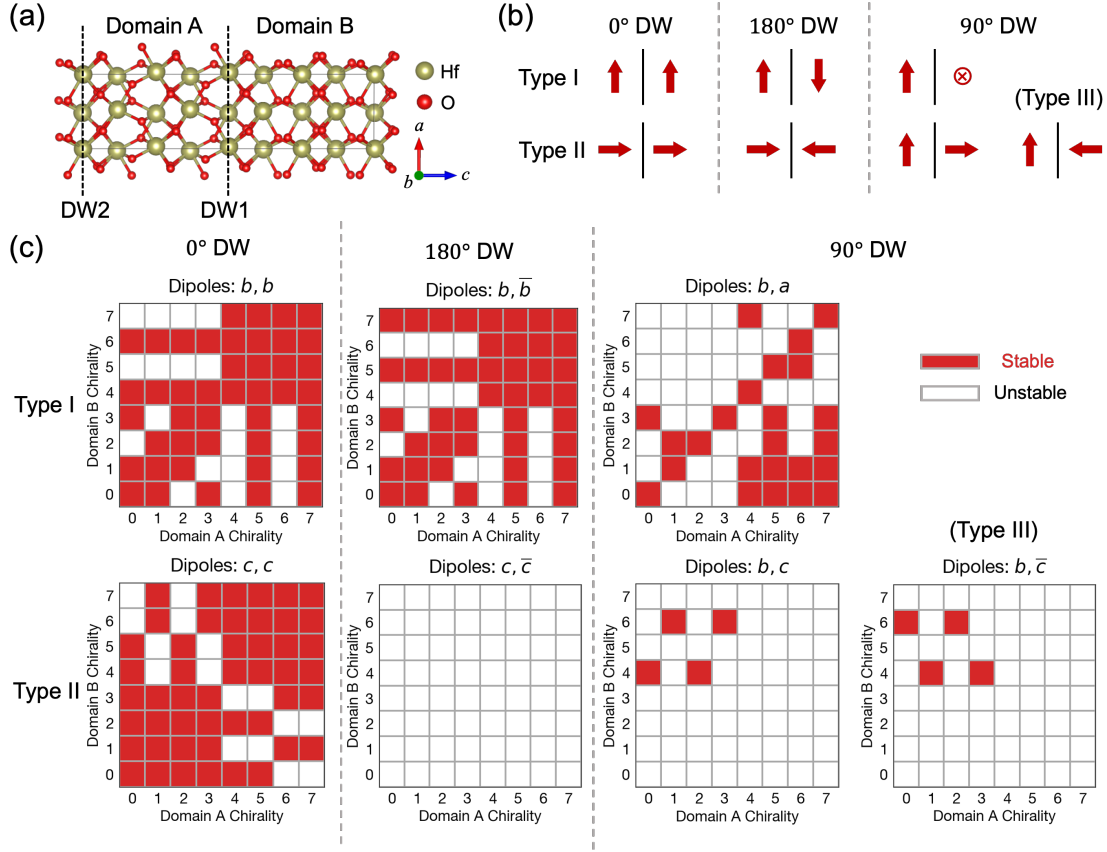


FIG. 1. Dependence of OIII domain wall stability on interface phonon modes. (a) The domain wall model with two domains. (b) Polarization configuration, and different types of 0° , 180° , 90° domain walls. (c) Dependence of OIII domain wall stability on interface phonon modes, or pseudo-chirality number at interface. The x-axis and y-axis of each stability map are the pseudo-chirality number of domain A and B in subfigure a. The figure title of each stability map shows the dipole configuration of domain A and B. The overlined axis is the compact notation for the reversed axis direction, e.g. \bar{c} means $-c$.

rized switching mechanisms of OIII phase in Fig. 3a [45]. Most of the switching paths follow the tetragonal ($P4_2/nmc$) mechanism of paths numbered one to three in the figure [45], therefore, we used this mechanism to study the switching of DW. We constructed single-domain structure and structures with some of the cells reversed shown in Fig. 3d, and calculated their transition paths in Fig. 3b. The first path is from the ground state of single-domain structure to the structure with two cells switched, for the structure with one unitcell switched is not stable. This path can be seen as the ferroelectric switching starting

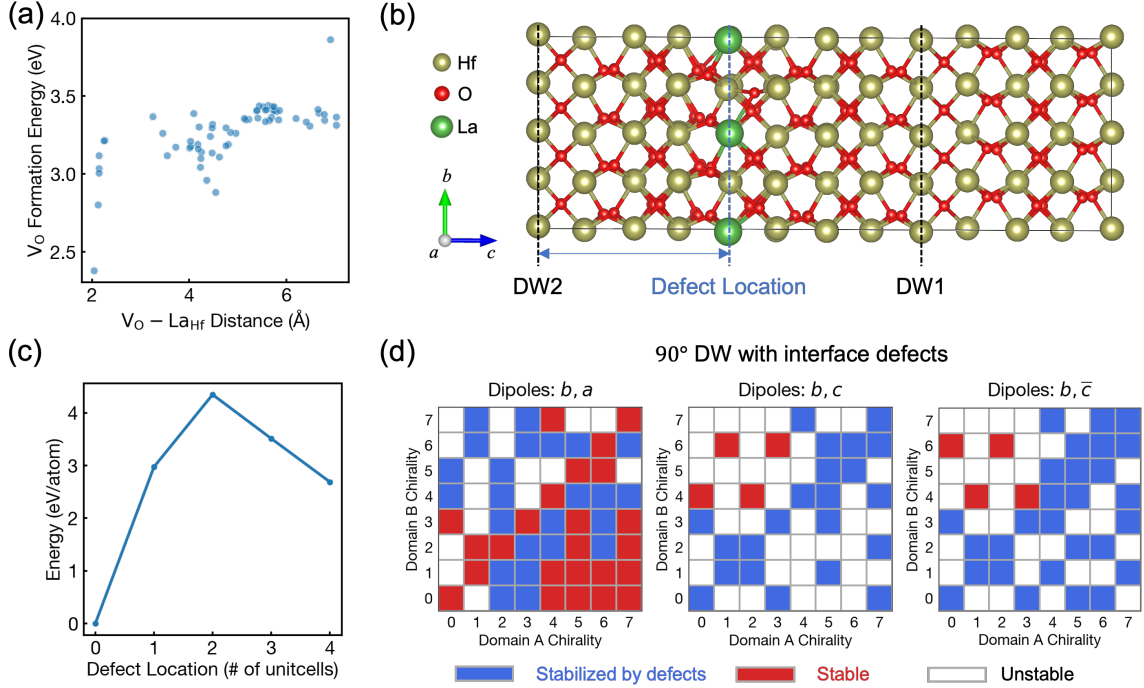


FIG. 2. Effects of defects on DWs. (a) Dependence of the formation energy of La substitutional defect La_{Hf} and oxygen vacancy V_O pairs on their distance, exhibiting a positive correlation, with the minimum formation energy achieved at the minimum distance. (b) The structure model used to study the dependence of DW energy on the distribution of defects. We put La_{Hf} and V_O defects in one of the domains with varying distances to the DW interface. (c) Dependence of energy of the model in subfigure b on the distance from the defects to DW interface. The energy is the lowest when the defects are at the interface, which indicates that the DW interfaces are more likely to form in the area with high defect density. (d) Dependence of stability of 90° DW with defects on interface phonon modes, or pseudo-chirality number at interface. We use different colors to distinguish the DWs that are stable with or without defects (blue) and the DWs that are unstable without defects but stable with defects (green).

from inside the domain, due to the periodic boundary condition used in calculation. The second path is from the single-domain structure with two cells switched to that with three cells switched, corresponding to the DW motion. We can see that the barrier is very large to switch from single domain, but becomes lower than the switching barrier between OIII phases once two cells are switched. These facts have three origins: the cells switched starting from single domain should be at least two, which raises the barrier, for the structure

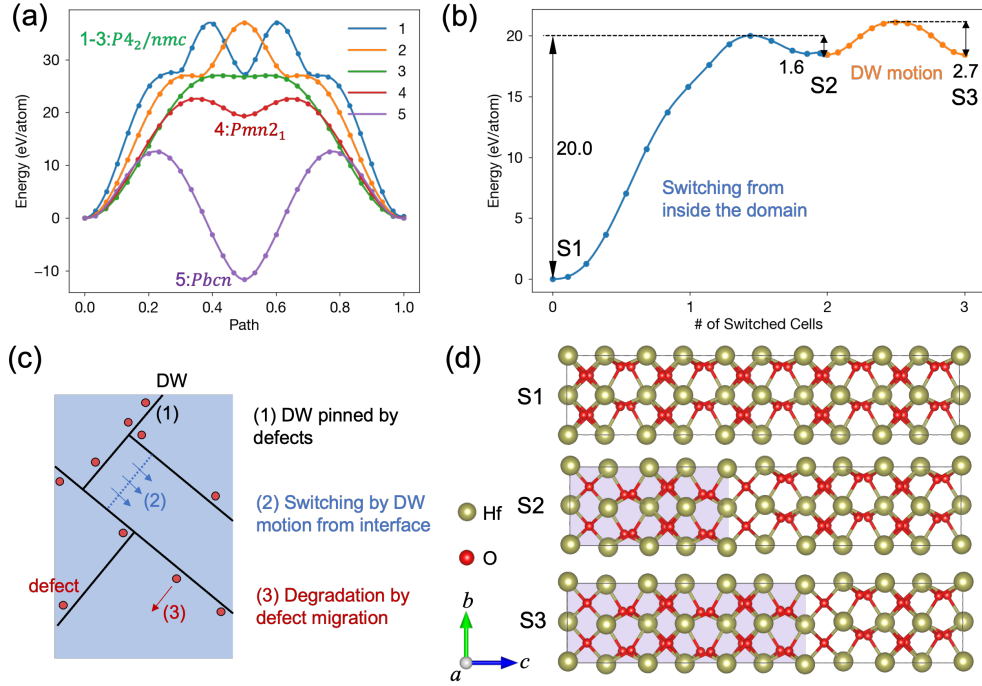


FIG. 3. Ferroelectric switching mechanism based on DW motion. (a) Summary of five switching paths of OIII phase. (b) The switching path from S1 to S2, and the path from S2 to S3. The two paths correspond to the switching from inside the domain and the DW motion. The structures of S1 to S3 are shown in subfigure c. (c) Schematic of proposed switching mechanism. (d) Structures in the switching paths in subfigure b: S1, the single-domain ground state; S2, a two-cell-reversed state; S3, a three-cell-reversed state.

with one cell switched is not stable; the switching from single domain introduces strain; the DW motion involves the interaction of modes at the interface only, compared with the switching path of OIII phase which requires the collective motion of all the modes in cells. We conjecture that the switching of DW mostly starts from the interface of DWs, because the defects distributed near the DW interface can lower the switching barrier significantly, similar to the case of OIII switching [46–48].

To visualize the domain structure and verify the stabilizing effect of defects such as oxygen vacancies, lanthanum-doped hafnium oxide (HLO) films were fabricated on TiO_2 films by atomic layer deposition (ALD). Fig. 4a shows the typical polarization–voltage (P–V) loops of the $TiN/HLO/TiO_2$ structure measured at 10 kHz, which exhibits the excellent ferroelectric properties of HLO. Grazing incidence X-ray diffraction (GIXRD) was employed to determine

the phase composition of HLO films. The diffraction pattern (Fig. 4b) demonstrates a dominant (111)-oriented OIII phase, which is crucial for ferroelectricity, alongside a minor M phase. To elucidate the elemental distribution of OIII phase, scanning transmission electron microscopy (STEM) high-angle annular dark field (HAADF) imaging combined with electron energy loss spectroscopy (EELS) analysis were performed along the O-[011] zone axis. Quantitative analysis of La and O energy loss spectra (Fig. 4d) reveals distinct compositional variations: black regions correspond to uniform La doping, while red regions indicate La-enriched domains. The corresponding background-subtracted O-K edge (Fig. 4e) further represent the fine structural differences driven by V_O . Oxygen vacancies modify the local crystal symmetry and electronic structure by influencing the hybridization between O-2p and Hf-d/La-d orbitals. The presence of V_O introduces shallow donor states below the conduction band, altering the relative intensities of peak A ($\sim 534\text{eV}$) and peak B ($\sim 537\text{eV}$) [56]. The significantly lower intensities of A/B peaks in the La-enriched (red) region suggest a correlation between higher La doping and increased oxygen vacancy concentration. This relationship can be understood through the charge compensation mechanism: the substitution of Hf^{4+} by La^{3+} creates a net negative charge that must be compensated by oxygen vacancies to maintain charge neutrality.

Atomic-resolution STEM imaging along the O-[001] zone axis was conducted to further examine the phase distribution and domain structure. This orientation is selected to enhance the visibility of oxygen displacements, facilitating the identification of polymorphs and domain boundaries. As shown in Fig. 4f-g, OIII ferroelectric domains are separated by 90° DW, with a minor fraction of M phase domains coexists at the interfaces. Fig. 4g reveals three distinct OIII ferroelectric domains separated by two types of domain walls. The DW1 is oriented along the O-[100]/O-[010] plane, while DW2 lies in the O-[110] plane. The stability of these domain walls is enhanced by the preferential segregation of La dopants and associated V_O . The EELS line scans of La distribution (Fig. 4h-i) reveal that both DW1 and DW2 exhibit significantly higher La concentrations compared to the bulk domains. According to the lowest-energy configuration, the formation of $\text{La}_{\text{Hf}}\text{-}V_O$ complexes enhances the stability of the DW interfaces. These initial defects are randomly distributed. This stands in contrast to the previous research results in fatigued structures, where the formation of periodic V_O led to degraded ferroelectricity[57]. This comparison indicates that a randomized vacancy distribution, rather than a periodic one, is crucial for stabilizing domain walls

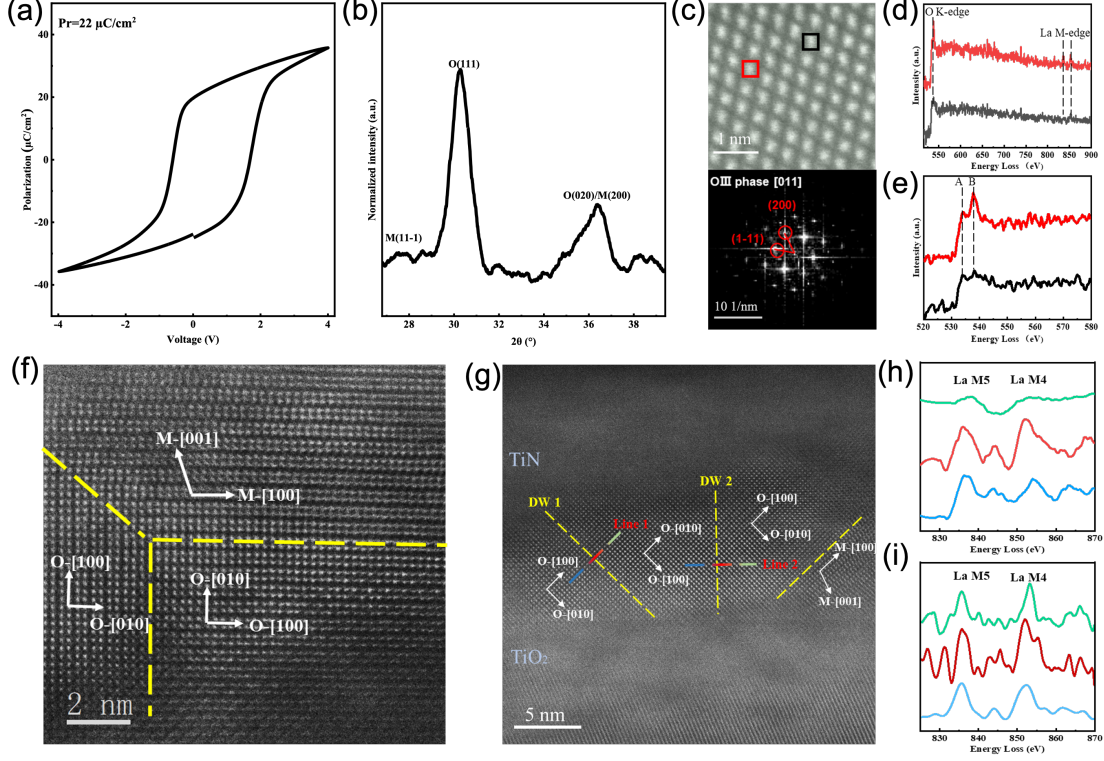


FIG. 4. Structural characterization and defect analysis of HfO₂ films. (a) P-V hysteresis loop of the TiN/HfO₂/TiO₂ stack showing a low coercive voltage of $2V_c = 2.3V$ and the remanent polarization of $P_r = 22\mu C/cm^2$. (b) GIXRD patterns of HfO₂ film. (c) STEM-HAADF image and corresponding fast-Fourier-transformation (FFT) patterns. (d) EELS spectra and (e) O-K edges obtained from the region marked with red line and black line in (c). (f) Atomic structures of HfO₂ film. (g) The coexistence of O domains with DWs in a single grain. La-M edges of (h) Line1 and (i) Line2 obtained from the DW1 and DW2. Each spectrum color corresponds to similar color position marked in (g).

and maintaining robust ferroelectric switching.

In summary, we systematically studied the DW stability and the effects of defects on DWs in ferroelectric La-doped HfO₂. We developed a method based on phonon mode expansion to classify the symmetrically inequivalent DWs, and carried out first principle calculations. We found that the oxygen vacancies are distributed near the La dopants and the defects have a pinning effect on the DW interface (Fig. 3c), which is confirmed by EELS and STEM experiments (Fig. 4). The stability of DWs depends on pseudo-chiralities of domains, or the interface phonon modes. The defects can increase the overall stability of DWs with

varying interface phonon modes. The DW structures stabilized by defects lead to the robust ferroelectricity in La-doped HfO_2 , and also facilitate ferroelectric switching through domain wall motion mechanism shown in Fig. 3c. The switching barrier can be lowered by the defects concentrated near the DW interface. These findings provide the microscopic origin for the enhanced ferroelectricity in HfO_2 by doping and defect engineering, which may provide guidance for the device optimization, especially the ferroelectric cycling behaviors which may be explained by the interplay between defects and DWs. There are experimental evidences showing that the defects can move during field cycling [30, 52, 54]. We conjectured that the defects may have an ordered distribution after a large number of field cycling, accompanied by the generation of more oxygen vacancies. This redistributed defects may lose the pinning and stabilization effects, leading to the transition from OIII phase to a monoclinic phase with defects which is polar but not switchable [12, 57]. This defect-induced phase transition may be one of the causes of the imprint effect and fatigue effect.

First Principle Method

Structure relaxation of DW model in Fig. 1a was carried out by first-principle calculation implemented in VASP software [49, 50]. Chemical species were treated using the projector-augmented plane wave method [58], with $5p^66s^25d^2$ valence electron configuration for Hf and $2s^22p^4$ for O. The plane wave cutoff energy was 600 eV and the Brillouin zone was sampled with gamma-centered k-point meshes with resolution 0.04. Exchange-correlation functional was approximated by the Perdew-Burke-Ernzerhof functional (PBE) [59] in generalized gradient approximation (GGA). The atom force convergence threshold was set to $0.01\text{eV}/\text{\AA}$ and energy convergence threshold was set to 10^{-6}eV .

DW model has one unitcell in a and b axis directions, and four unitcells in c axis direction, with two unitcells belonging to domain A and the other two belonging to domain B. The DW model with defects has two unitcells in a and b axis directions, and four unitcells in c axis direction, with two unitcells belonging to domain A and the other two belonging to domain B. The DW model has two domain wall interfaces as shown in Fig. 1a. 25% of the Hf atoms at each DW interface are substituted by La atoms, and one oxygen vacancy per two La substitutional defects is introduced to compensate charges. The oxygen vacancy is adjacent to one of the La dopants.

All the structures in figures were visualized using VESTA software [60].

Film Fabrication

The TiN/HLO/TiO₂ heterostructure investigated in this work was previously reported by our group [61] (Fig. S1). Initially, an 8-nm-thick TiO₂ was deposited via ALD using TiCl₄ precursor and O₃ as oxidant at 300°C. The TiO₂ film was crystallized through rapid thermal annealing (RTA) at 600°C for 30 s in N₂ atmosphere. Following this process, an 8-nm-thick La-doped HfO₂ film was deposited using atomic layer deposition (ALD) with Hf[N(C₂H₅)CH₃]₄, La(C₁₁H₁₉O₂)₃ precursors and O₃ as oxidant at 300°C. The Hf:La ratio was controlled to be 11:1 by adjusting the ALD cycle ratio of HfO₂ and La₂O₃, as confirmed by energy dispersive spectroscopy (EDS) analysis (Fig. S2). Subsequently, a 40-nm-thick TiN film was deposited by physical vapor deposition (PVD). Finally, the TiN/HLO/TiO₂ stack underwent RTA at 600°C for 30 s in N₂ atmosphere to promote crystallization.

Experimental Characterization

P-V hysteresis loop of the TiN/HLO/TiO₂ stack was measured using 10 kHz triangular pulse with amplitude of 4 V applied to the TiN top electrode while the TiO₂ bottom layer was grounded.

Structural characterization of the stack was performed using grazing-incidence-angle XRD (GIXRD) instrument (Smartlab) operated at 150 mA and 50 kV. The incidence angle was fixed at 2°, and scanning speed was 4°/min. The overall and atomic structures of the HLO layers were examined by high-angle annular dark-field scanning transmission electron microscopy (HAADF-STEM) using a Cs-corrected microscope operated at 300 kV (JEM-ARM300F2 FHP, JEOL). The collection angle range of the HAADF and annular bright-field (ABF) detectors were 64-180 mrad and 12-24 mrad, respectively. Atomic-scale HAADF-STEM images were processed using a Wiener filtering method (Radial Wiener Filter) to reduce random background noise. Electron energy-loss spectroscopy (EELS) spectral imaging data for the HLO samples were recorded over an energy range of 500–900 eV, which encompassed the O K and La M edges, using a Gatan EELS spectrometer. The apparatus had an entrance aperture of 5 mm and an energy dispersion of 0.3 eV per channel.

This work is supported by the National Natural Science Foundation of China (Grants No. T2293703, No. T2293700).

* These authors contributed equally to this work.

† feiliu@pku.edu.cn

‡ xiwei@tju.edu.cn

§ kangjf@pku.edu.cn

- [1] T. Böske, J. Müller, D. Bräuhäus, U. Schröder, and U. Böttger, Ferroelectricity in hafnium oxide thin films, *Applied Physics Letters* **99**, 102903 (2011).
- [2] J. Müller, E. Yurchuk, T. Schlösser, J. Paul, R. Hoffmann, S. Müller, D. Martin, S. Slesazek, P. Polakowski, J. Sundqvist, M. Czernohorsky, K. Seidel, P. Kücher, R. Boschke, M. Trentzsch, K. Gebauer, U. Schröder, and T. Mikolajick, Ferroelectricity in $\text{hfo}<inf>2</inf>$ enables nonvolatile data storage in 28 nm hkmg, in *2012 Symposium on VLSI Technology (VLSIT)* (IEEE) pp. 25–26.

- [3] A. Chernikova, M. Kozodaev, A. Markeev, D. Negrov, M. Spiridonov, S. Zarubin, O. Bak, P. Buragohain, H. Lu, E. Suvorova, A. Gruverman, and A. Zenkevich, Ultrathin hf0.5zr0.5o2 ferroelectric films on si, *ACS Applied Materials & Interfaces* **8**, 7232 (2016).
- [4] M. H. Park, Y. H. Lee, H. J. Kim, Y. J. Kim, T. Moon, K. D. Kim, J. Mueller, A. Kersch, U. Schroeder, and T. Mikolajick, Ferroelectricity and antiferroelectricity of doped thin hfo2-based films, *Advanced Materials* **27**, 1811 (2015).
- [5] J. Okuno, T. Kunihiro, K. Konishi, H. Maemura, Y. Shuto, F. Sugaya, M. Materano, T. Ali, K. Kuehnel, K. Seidel, U. Schroeder, T. Mikolajick, M. Tsukamoto, and T. Umebayashi, Soc compatible 1t1c feram memory array based on ferroelectric hf0.5zr0.5o2, in *2020 IEEE Symposium on VLSI Technology (IEEE)* pp. 1–2.
- [6] Q. Luo, T. Gong, Y. Cheng, Q. Zhang, H. Yu, J. Yu, H. Ma, X. Xu, K. Huang, and X. Zhu, Hybrid 1t e-dram and e-nvm realized in one 10 nm node ferro finfet device with charge trapping and domain switching effects, in *2018 IEEE International Electron Devices Meeting (IEDM) (IEEE)* pp. 2.6.1–2.6.4.
- [7] S. S. Cheema, D. Kwon, N. Shanker, R. dos Reis, S.-L. Hsu, J. Xiao, H. Zhang, R. Wagner, A. Datar, M. R. McCarter, C. R. Serrao, A. K. Yadav, G. Karbasian, C.-H. Hsu, A. J. Tan, L.-C. Wang, V. Thakare, X. Zhang, A. Mehta, E. Karapetrova, R. V. Chopdekar, P. Shafer, E. Arenholz, C. Hu, R. Proksch, R. Ramesh, J. Ciston, and S. Salahuddin, Enhanced ferroelectricity in ultrathin films grown directly on silicon, *Nature* **580**, 478 (2020).
- [8] T. D. Huan, V. Sharma, G. A. Rossetti, and R. Ramprasad, Pathways towards ferroelectricity in hafnia, *Physical Review B* **90**, 064111 (2014).
- [9] Y. Wei, P. Nukala, M. Salverda, S. Matzen, H. J. Zhao, J. Momand, A. S. Everhardt, G. Agnus, G. R. Blake, P. Lecoer, B. J. Kooi, J. Íñiguez, B. Dkhil, and B. Noheda, A rhombohedral ferroelectric phase in epitaxially strained hf0.5zr0.5o2 thin films, *Nature Materials* **17**, 1095 (2018).
- [10] Y. Wang, L. Tao, R. Guzman, Q. Luo, W. Zhou, Y. Yang, Y. Wei, Y. Liu, P. Jiang, Y. Chen, S. Lv, Y. Ding, W. Wei, T. Gong, Y. Wang, Q. Liu, S. Du, and M. Liu, A stable rhombohedral phase in ferroelectric hf(zr)_{1+x}o₂ capacitor with ultralow coercive field, *Science* **381**, 558 (2023).
- [11] C. Liu, F. Liu, Q. Luo, P. Huang, X. Xu, H. Lv, Y. Zhao, X. Liu, and J. Kang, Role of oxygen vacancies in electric field cycling behaviors of ferroelectric hafnium oxide, in *2018*

- IEEE International Electron Devices Meeting (IEDM)* (IEEE) pp. 16.4. 1–16.4. 4.
- [12] C. Yu, H. Ma, M. Li, F. Liu, X. Ding, Y. Zhao, H. Li, X. Song, F. Liu, W. Yang, J. Xu, J. Zhang, X. Hao, L. Liu, P. Huang, P. Gao, and J. Kang, Insights into the origin of robust ferroelectricity in hfo₂-based thin films from the order-disorder transition driven by vacancies, *Physical Review Applied* **22**, 024028 (2024).
- [13] T. Zhu, L. Ma, S. Deng, and S. Liu, Progress in computational understanding of ferroelectric mechanisms in hfo₂, *npj Computational Materials* **10**, 188 (2024).
- [14] Z. Fan, J. Chen, and J. Wang, Ferroelectric hfo₂-based materials for next-generation ferroelectric memories, *Journal of Advanced Dielectrics* **6**, 1630003 (2016).
- [15] U. Schroeder, M. H. Park, T. Mikolajick, and C. S. Hwang, The fundamentals and applications of ferroelectric hfo₂, *Nature Reviews Materials* **7**, 653 (2022).
- [16] W. Yang, C. Yu, H. Li, M. Fan, X. Song, H. Ma, Z. Zhou, P. Chang, P. Huang, F. Liu, X. Liu, and J. Kang, Ferroelectricity of hafnium oxide-based materials: Current status and future prospects from physical mechanisms to device applications, *Journal of Semiconductors* **44**, 053101 (2023).
- [17] P. Fan, Y. K. Zhang, Q. Yang, J. Jiang, L. M. Jiang, M. Liao, and Y. C. Zhou, Origin of the intrinsic ferroelectricity of hfo₂ from ab initio molecular dynamics, *The Journal of Physical Chemistry C* **123**, 21743 (2019).
- [18] O. Ohtaka, H. Fukui, T. Kunisada, T. Fujisawa, K. Funakoshi, W. Utsumi, T. Irifune, K. Kuroda, and T. Kikegawa, Phase relations and volume changes of hafnia under high pressure and high temperature, *Journal of the American Ceramic Society* **84**, 1369 (2001).
- [19] M. Hyuk Park, H. Joon Kim, Y. Jin Kim, T. Moon, and C. Seong Hwang, The effects of crystallographic orientation and strain of thin hf_{0.5}zr_{0.5}o₂ film on its ferroelectricity, *Applied Physics Letters* **104**, 072901 (2014).
- [20] S. Zhou, J. Zhang, and A. M. Rappe, Strain-induced antipolar phase in hafnia stabilizes robust thin-film ferroelectricity, *Science Advances* **8**, eadd5953 (2022).
- [21] R. Batra, T. D. Huan, J. L. Jones, G. Rossetti, and R. Ramprasad, Factors favoring ferroelectricity in hafnia: A first-principles computational study, *The Journal of Physical Chemistry C* **121**, 4139 (2017).
- [22] S. Liu and B. M. Hanrahan, Effects of growth orientations and epitaxial strains on phase stability of hfo₂ thin films, *Physical Review Materials* **3**, 054404 (2019).

- [23] E. D. Grimley, T. Schenk, T. Mikolajick, U. Schroeder, and J. M. LeBeau, Atomic structure of domain and interphase boundaries in ferroelectric hfo₂, *Advanced Materials Interfaces* **5**, 1701258 (2018).
- [24] M. H. Park, Y. H. Lee, H. J. Kim, T. Schenk, W. Lee, K. D. Kim, F. P. G. Fengler, T. Mikolajick, U. Schroeder, and C. S. Hwang, Surface and grain boundary energy as the key enabler of ferroelectricity in nanoscale hafnia-zirconia: a comparison of model and experiment, *Nanoscale* **9**, 9973 (2017).
- [25] J. Müller, T. S. Böske, U. Schröder, S. Mueller, D. Bräuhaus, U. Böttger, L. Frey, and T. Mikolajick, Ferroelectricity in simple binary zro₂ and hfo₂, *Nano Letters* **12**, 4318 (2012).
- [26] X. Xu, F.-T. Huang, Y. Qi, S. Singh, K. M. Rabe, D. Obeysekera, J. Yang, M.-W. Chu, and S.-W. Cheong, Kinetically stabilized ferroelectricity in bulk single-crystalline hfo₂:y, *Nature Materials* **20**, 826 (2021).
- [27] U. Schroeder, E. Yurchuk, J. Muller, D. Martin, T. Schenk, P. Polakowski, C. Adelman, M. I. Popovici, S. V. Kalinin, and T. Mikolajick, Impact of different dopants on the switching properties of ferroelectric hafniumoxide, *Japanese Journal of Applied Physics* **53**, 85 (2014).
- [28] Y. Zhou, Y. K. Zhang, Q. Yang, J. Jiang, P. Fan, M. Liao, and Y. C. Zhou, The effects of oxygen vacancies on ferroelectric phase transition of hfo₂-based thin film from first-principle, *Computational Materials Science* **167**, 143 (2019).
- [29] L.-Y. Ma and S. Liu, Structural polymorphism kinetics promoted by charged oxygen vacancies in hfo₂, *Physical Review Letters* **130**, 096801 (2023).
- [30] S. Starschich, S. Menzel, and U. Böttger, Evidence for oxygen vacancies movement during wake-up in ferroelectric hafnium oxide, *Applied Physics Letters* **108**, 032903 (2016).
- [31] A. Kashir, S. Oh, and H. Hwang, Defect engineering to achieve wake-up free hfo₂-based ferroelectrics, *Advanced Engineering Materials* **23**, 2000791 (2021).
- [32] D.-H. Choe, S. Kim, T. Moon, S. Jo, H. Bae, S.-G. Nam, Y. S. Lee, and J. Heo, Unexpectedly low barrier of ferroelectric switching in hfo₂ via topological domain walls, *Materials Today* **50**, 8 (2021).
- [33] W. Ding, Y. Zhang, L. Tao, Q. Yang, and Y. Zhou, The atomic-scale domain wall structure and motion in hfo₂-based ferroelectrics: A first-principle study, *Acta Materialia* **196**, 556 (2020).
- [34] Y. Qi, S. Singh, and K. M. Rabe, Polarization switching in ferroelectric hfo₂ from first-

- principles lattice mode analysis, *Physical Review B* **111**, 134106 (2025).
- [35] G.-D. Zhao, X. Liu, W. Ren, X. Zhu, and S. Yu, Symmetry of ferroelectric switching and domain walls in hafnium dioxide, *Physical Review B* **106**, 064104 (2022).
- [36] P. Kumar, D. Gupta, and J. H. Lee, Negative gradient energy facilitates charged domain walls in hfo₂, *Physical Review Letters* **134**, 166101 (2025).
- [37] T. K. Paul, A. K. Saha, and S. K. Gupta, Formation and energetics of head-to-head and tail-to-tail domain walls in hafnium zirconium oxide, *Scientific Reports* **14**, 9861 (2024).
- [38] Y.-C. Li, Z. Xu, X.-X. Li, Y. Wu, X.-N. Zhu, Z. Ji, M. Li, H.-L. Lu, D. W. Zhang, and R. Huang, Unveiling the role of domain wall propagation in enhancing switching properties of ferroelectric ga-doped hfo₂ thin films, *Materials Today Chemistry* **49**, 103091 (2025).
- [39] K. Park, D. Kim, K. Lee, H.-J. Lee, J. Kim, S. Kang, A. Lin, A. J. Pattison, W. Theis, C. H. Kim, H. Choi, J. W. Cho, P. Ercius, J. H. Lee, S. C. Chae, and J. Park, Atomic-scale scanning of domain network in the ferroelectric hfo₂ thin film, *ACS Nano* **18**, 26315 (2024).
- [40] A. S. Foster, F. Lopez Gejo, A. L. Shluger, and R. M. Nieminen, Vacancy and interstitial defects in hafnia, *Physical Review B* **65**, 174117 (2002).
- [41] M. Materano, P. D. Lomenzo, A. Kersch, M. H. Park, T. Mikolajick, and U. Schroeder, Interplay between oxygen defects and dopants: effect on structure and performance of hfo₂-based ferroelectrics, *Inorganic Chemistry Frontiers* **8**, 2650 (2021).
- [42] H.-J. Lee, M. Lee, K. Lee, J. Jo, H. Yang, Y. Kim, S. C. Chae, U. Waghmare, and J. H. Lee, Scale-free ferroelectricity induced by flat phonon bands in hfo₂, *Science* **369**, 1343 (2020).
- [43] S. Y. Fan, S. Singh, X. H. Xu, K. Park, Y. B. Qi, S. W. Cheong, D. Vanderbilt, K. M. Rabe, and J. L. Musfeldt, Vibrational fingerprints of ferroelectric hfo₂, *Npj Quantum Materials* **7**, ARTN 32 10.1038/s41535-022-00436-8 (2022).
- [44] M. Kingsland, S. Lisenkov, S. Najmaei, and I. Ponomareva, Phase transitions in hfo₂ probed by first-principles computations, *Journal of Applied Physics* **135**, 10.1063/5.0180064 (2024).
- [45] Note1, (2025), please see our paper on arXiv entitled Decoding the Complexity of Ferroelectric Orthorhombic HfO₂: A Unified Mode Expansion Approach.
- [46] H. Yang, H.-J. Lee, J. Jo, C. H. Kim, and J. H. Lee, Role of si doping in reducing coercive fields for ferroelectric switching in hfo₂, *Physical Review Applied* **14**, 064012 (2020).
- [47] K. Lee, K. Park, H.-J. Lee, M. S. Song, K. C. Lee, J. Namkung, J. H. Lee, J. Park, and S. C. Chae, Enhanced ferroelectric switching speed of si-doped hfo₂ thin film tailored by oxygen

- deficiency, *Scientific Reports* **11**, 6290 (2021).
- [48] S. Clima, S. R. C. McMitchell, K. Florent, L. Nyns, M. Popovici, N. Ronchi, L. D. Piazza, J. V. Houdt, and G. Pourtois, First-principles perspective on poling mechanisms and ferroelectric/antiferroelectric behavior of $\text{Hf}_{1-x}\text{Zr}_x\text{O}_2$ for FeFET applications, in *2018 IEEE International Electron Devices Meeting (IEDM)*, pp. 16.5.1–16.5.4.
- [49] G. Kresse and J. Hafner, Ab initio molecular dynamics for liquid metals, *Physical Review B* **47**, 558 (1993).
- [50] G. Kresse and J. Furthmüller, Efficient iterative schemes for ab initio total-energy calculations using a plane-wave basis set, *Physical Review B* **54**, 11169 (1996).
- [51] J. Yang, J. Liao, J. Huang, F. Yan, M. Liao, and Y. Zhou, Kinetic phase transition paths and phase stability in ferroelectric HfO_2 , *Scripta Materialia* **242**, 115953 (2024).
- [52] P. Nukala, M. Ahmadi, Y. Wei, S. de Graaf, E. Stylianidis, T. Chakraborty, S. Matzen, W. Zandbergen Henny, A. Björling, D. Mannix, D. Carbone, B. Kooi, and B. Noheda, Reversible oxygen migration and phase transitions in hafnia-based ferroelectric devices, *Science* **372**, 630 (2021).
- [53] R. Materlik, C. Künneth, M. Falkowski, T. Mikolajick, and A. Kersch, Al-, y-, and la-doping effects favoring intrinsic and field induced ferroelectricity in HfO_2 : A first principles study, *Journal of Applied Physics* **123**, 164101 (2018).
- [54] J. Chen, C. Jin, X. Yu, X. Jia, Y. Peng, Y. Liu, B. Chen, R. Cheng, and G. Han, Impact of oxygen vacancy on ferroelectric characteristics and its implication for wake-up and fatigue of HfO_2 -based thin films, *IEEE Transactions on Electron Devices* **69**, 5297 (2022).
- [55] L. Ma, J. Wu, T. Zhu, Y. Huang, Q. Lu, and S. Liu, Ultrahigh oxygen ion mobility in ferroelectric hafnia, *Physical Review Letters* **131**, 256801 (2023).
- [56] J. Lee, M. S. Song, W.-S. Jang, J. Byun, H. Lee, M. H. Park, J. Lee, Y.-M. Kim, S. C. Chae, and T. Choi, Modulating the ferroelectricity of hafnium zirconium oxide ultrathin films via interface engineering to control the oxygen vacancy distribution, *Advanced Materials Interfaces* **9**, 2101647 (2022).
- [57] K. Z. Rushchanskii, S. Blügel, and M. Ležaić, Ordering of oxygen vacancies and related ferroelectric properties in $\text{HfO}_{2-\delta}$, *Physical Review Letters* **127**, 087602 (2021).
- [58] P. E. Blöchl, Projector augmented-wave method, *Physical review B* **50**, 17953 (1994).
- [59] J. P. Perdew, K. Burke, and M. Ernzerhof, Generalized gradient approximation made simple,

- Physical Review Letters **77**, 3865 (1996).
- [60] K. Momma and F. Izumi, Vesta 3 for three-dimensional visualization of crystal, volumetric and morphology data, Journal of Applied Crystallography **44**, 1272 (2011).
- [61] X. Song, C. Yu, J. Zhang, H. Yang, S. Li, D. Sun, H. Zhu, X. Xiao, Z. Zhou, P. Huang, X. Zhang, X. Liu, and J. Kang, First demonstration of double-gated ferroelectric field-effect-transistor with TiO₂ channel for multi-level storage, IEEE Electron Device Letters **46**, 1329 (2025).

Supplemental Materials: Domain Walls Stabilized by Intrinsic Phonon Modes and Engineered Defects Enable Robust Ferroelectricity in HfO₂

The Supplementary material includes STEM and EDS experiment results of our film.

Characterization of the TiN/HfO₂/TiO₂ structure and element distribution was conducted using STEM (Fig. S1) and EDS (Fig. S2). The STEM-HAADF images indicated that the TiN-HfO₂-TiO₂ heterointerface was coherent. To further investigate the element distribution relationships within HfO₂ films, atomic-resolution STEM-HAADF and STEM-ABF images were conducted along the O-[011] zone axis (Fig. S1b-c). STEM-HAADF technology is highly sensitive to the atomic number (Z) of the analyzed material. Elements with higher Z values exhibit stronger electron beam interactions with atomic nuclei, resulting in greater electron scattering at high angles. Due to the contrast difference between La ($Z=57$) and Hf ($Z=74$), La-enriched locations are thus identified (Fig. S1d). The STEM-ABF image is formed by weakly scattered electrons and has the advantage of higher sensitivity to light elements such as oxygen. It can also display heavier atoms. The ABF image corresponding to the position of the oxygen atom in the HAADF image is used to determine the distribution of oxygen vacancies (Fig. S1c). As shown in Fig. S1e, the number of oxygen atoms at the lanthanum-enriched position decreases, which also corresponds to the position with the lowest formation energy of oxygen vacancies in the calculated results.

Furthermore, STEM observations of HfO₂ crystal grain reveal different domain structures partitioned by 90° and 180° DWs (Fig. S3a). The oxygen atomic columns are clearly resolved in the STEM-ABF image (Fig. S3d). Specially, the three-fold coordinated atomic columns on the left shift along the O-[100] direction, while the opposing columns on the right shift along the O-[$\bar{1}00$] direction. This anti-parallel displacement confirms the existence of a 180° DW, as indicated by the dashed white line in Fig. S3c.

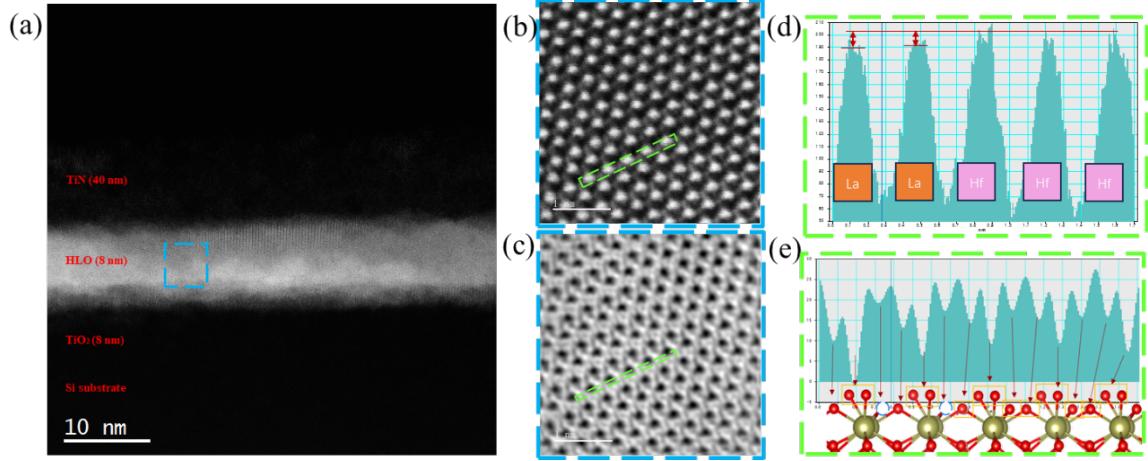


FIG. S1. Structural characterization of HLO film. (a) Cross-sectional HADDF image of TiN/HLO/TiO₂ stack. The HADDF (b) and ABF (c) images projected along O-[011] zone axis. The green lines indicate the extraction contrast positions. (d) The contrast curve is used to identify the positions of La atoms in the HLO film. (e) The contrast curve is used to identify the positions of oxygen atoms in the HLO film.

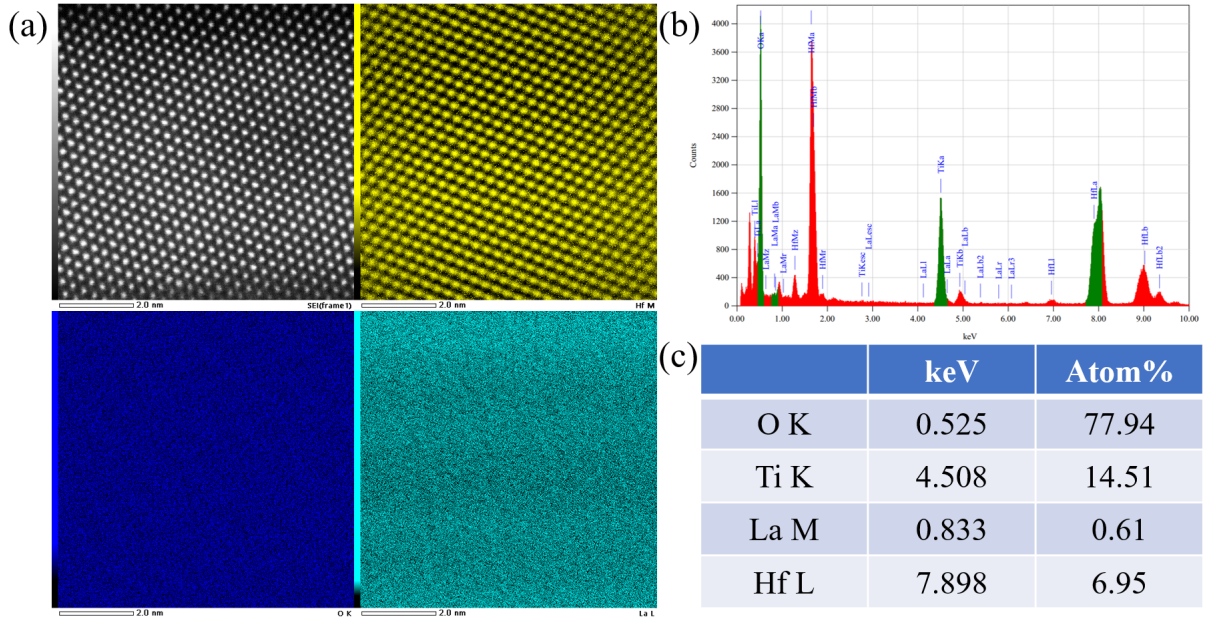


FIG. S2. Element distribution of HLO film. (a) EDS elemental mapping analysis. (b) X-ray spectra with O, Ti, La and Hf elements corresponding line. (c) The proportion of element contents in (b).

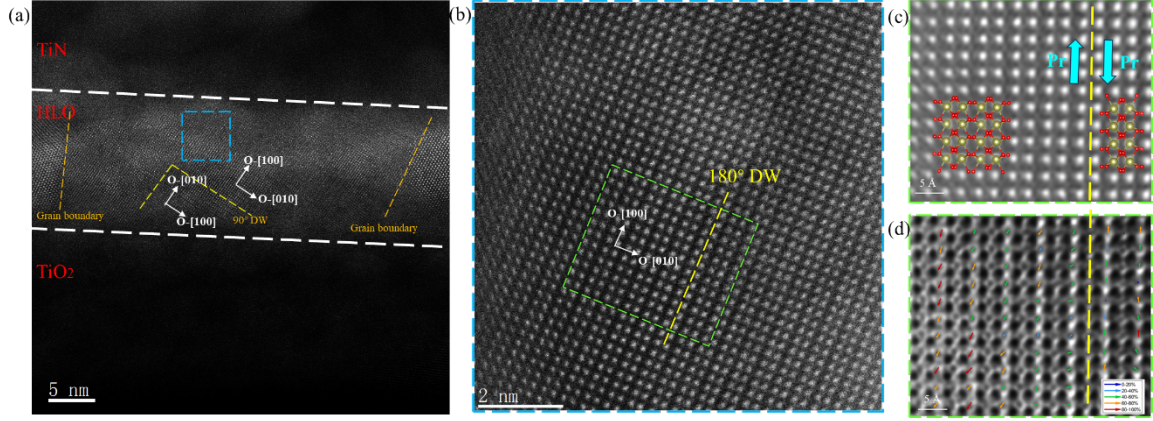


FIG. S3. STEM-images of the HLO film projected along O-[001] zone axis. (a) HLO grains can consist of different portions of ferroelectric domains and DWs. (b) HADDF image acquired from the blue square area in (a). (c) Enlarged drawings obtained from the selected green areas highlighted in (a), where the arrows indicate the corresponding direction of polarization. (d) Three-fold coordinated oxygen atom displacement vectors and 180° DW.